Magneto-Inductive Magnetic Resonance Imaging Duodenoscope

Richard R. A. Syms[1, *], Evdokia Kardoulaki[1], Marc Rea[2], Kaushal Choonee[3], Simon Taylor-Robinson[4], Christopher Wadsworth[4], and Ian R. Young[1]

Abstract—A magnetic resonance imaging (MRI) duodenoscope is demonstrated, by combining non-magnetic endoscope components with a thin-film receiver based on a magneto-inductive waveguide. The waveguide elements consist of figure-of-eight shaped inductors formed on either side of a flexible substrate and parallel plate capacitors that use the substrate as a dielectric. Operation is simulated using equivalent circuit models and by computation of two- and three-dimensional sensitivity patterns. Circuits are fabricated for operation at 127.7 MHz by double-sided patterning of copper-clad Kapton and assembled onto non-magnetic flexible endoscope insertion tubes. Operation is verified by bench testing and by ^{1}H MRI at 3T using phantoms. The receiver can form a segmented coaxial image along the length of the endoscope, even when bent, and shows a signal-to-noise-ratio advantage over a surface array coil up to three times the tube diameter at the tip. Initial immersion imaging experiments have been carried out and confirm an encouraging lack of sensitivity to RF heating.

1. INTRODUCTION

The signal-to-noise ratio (SNR) in magnetic resonance imaging (MRI) is limited by noise from the body, as well as the detection coil [1, 2]. Consequently, increased SNR can be obtained using coils with restricted fields of view (FOV), provided these match the target tissue [3], Many small internal coils have been developed for imaging lumens such as arteries, ducts and the gastrointestinal (GI) tract. For compatibility with clinical procedures these are normally based on endoscopes [4–6] or catheters [7–10], and devices for tracking have also been developed [11]. However, all must be decoupled from the B_1 field during excitation [12]. RF heating of linear conductors must also be avoided [13]; solutions include insertion of chokes or tank filters to suppress common-mode currents [14, 15], and transformer-segmentation [16, 17].

Many authors have also attempted to exploit the properties of metamaterials to increase SNR in MRI. Most involve external resonant relays, for example based on 'Swiss roll' resonators [18], magneto-inductive lenses [19, 20] or metasurfaces [21, 22]. Considerable efforts have also been made to develop endoscopes based on parallel wire media; however, demonstrated systems are still extremely bulky [23–25]. The closest analogue to conventional clinical tools is still the magneto-inductive (MI) catheter receiver [26–29]. This structure is based on a thin-film MI cable [30, 31], a flexible form of a MI waveguide [32, 33].

MI waveguides are inherently segmented, and combination with a figure-of-eight inductor shape introduces decoupling and patient safety [28]. Thin-film construction allows integration onto a hollow catheter using only heat-shrink tubing, yielding a disposable system compatible with endoscopic insertion over a guide wire [27]. Its sensitivity reduces with radial distance r as $1/r^2$, and although its reception pattern is also segmented, it can obtain an image along its whole length (2 m) even when

bent [26]. Comparison with external array coils has shown a SNR advantage up to several times the catheter diameter [29]. It may therefore have applications in high-resolution endolumenal imaging.

Experience with both systems suggests a third possibility, namely a magneto-inductive MR-imaging duodenoscope, which would combine the ease of use of an endoscope with a field-of-view encompassing much of the GI tract. Here we demonstrate an early prototype operating at 3T. Design is discussed in Section 2, and detection sensitivity in Section 3. Construction and electrical evaluation are described in Section 4, and magnetic resolution imaging experiments using phantoms in Section 5. Conclusions are drawn in Section 6.

2. DESIGN

We first consider electrical design and response. In contrast to earlier MR-imaging endoscopes [4–6], that provide an image only near a tip-mounted coil, the new instrument is intended to image the GI tract from the oesophagus to the duodenum. To achieve this, a receiver with a segmented, concentric cylindrical FOV is mounted along the length of the insertion tube, as shown in Figure 1(a). The tube is filled with a stack of discs pierced with channels for steering cables, imaging fibres, water/air and biopsy as shown in the longitudinal section of Figure 1(b). The receiver is constructed as a flexible thin-film circuit intended for mounting between the inner and outer sheath, with the conductors on a diameter as shown in the axial section of Figure 1(c).
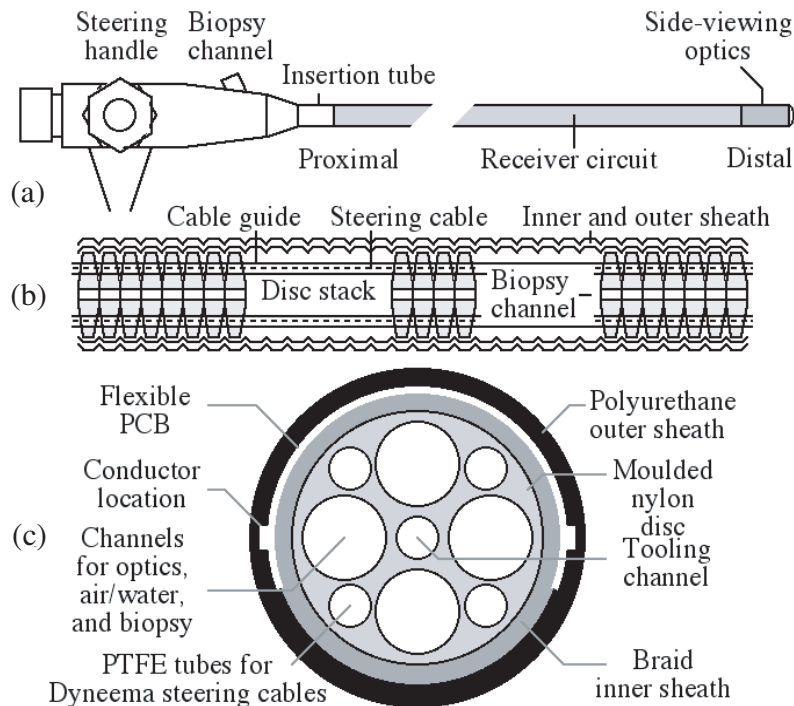
Figure 1. (a) Magneto-inductive MR-imaging endoscope; (b) and c) Longitudinal and axial sections of insertion tube.

2.1. Electrical Design

Figure 2(a) shows the circuit layout, which is based on a self-terminating MI waveguide [26, 29]. The main section is a regular array of L-C resonators, magnetically coupled to their nearest neighbours. Each element is constructed from a printed inductor (with adjacent inductors on either side of the substrate) and a pair of parallel plate capacitors that use the substrate as an interlayer. To allow tuning, capacitors are formed as strips at the circuit edge. At distal end, the waveguide is terminated with a loop having a
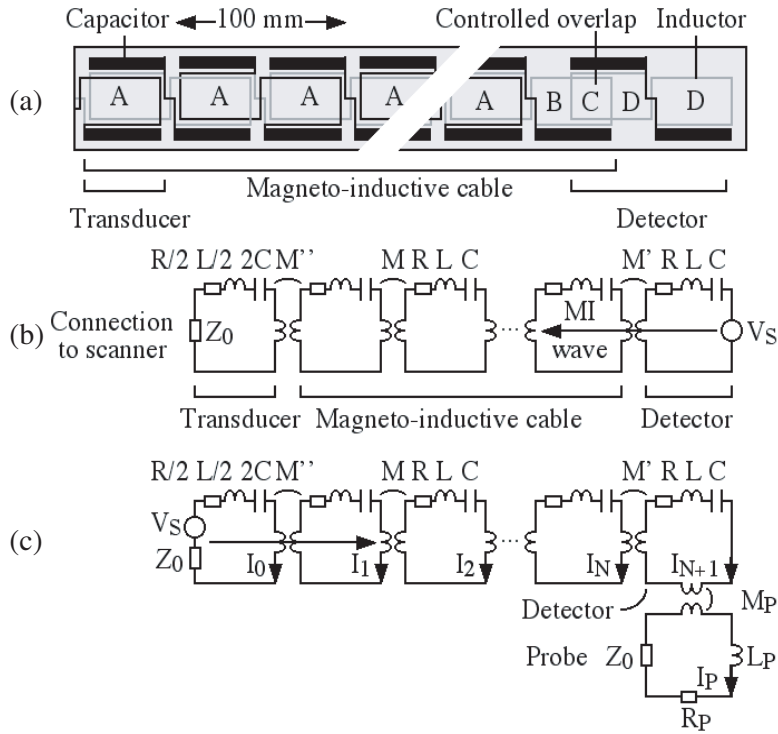
Figure 2. (a) Layout of magneto-inductive receiver; (b) and (c) Equivalent circuits for normal operation and testing.

controlled overlap with the last waveguide element. At the proximal end, it is connected to electronics via a transducer based on a halved element.

The sheath provides electrical insulation. To minimise coupling to the B_1 field during excitation, the inductors are figure-of-eight-shaped. Similarly, to minimise resonant coupling to the electric field, the length of each element is made less than half a wavelength for surface waves on wire immersed in tissue. The design is conservative, since the resonant length is increased by the low dielectric constant of the insertion tube.

Figure 2(b) shows the equivalent circuit. Each element has resistance R, inductance L and capacitance C and resonates at angular frequency $\omega_0 = 1/\sqrt{(LC)}$. Elements are coupled to their neighbours by a mutual inductance M, so the waveguide has a characteristic impedance $Z_{0M} = \omega_0 M$ at resonance. At the distal end, self-termination is achieved using a mutual inductance M' such that $\omega_0 M' = \sqrt{(Z_{0M}R)}$. At the proximal end, the waveguide is connected to a broadband transducer based on a halved element with inductance $L/2$ and capacitance 2C [31]. Matching to the scanner impedance Z_0 is achieved using a mutual inductance M'' such that $\omega_0 M'' = \sqrt{(Z_0 Z_{0M})}$.

Under these conditions a voltage signal V_S induced in the distal element by nuclear magnetic dipoles will excite a MI wave that travels to the proximal end without reflection. Of course, voltages may be induced in any element, so the circuit can detect MRI signals along its length [26]. However, sensitivity at the locations A ... D in Figure 2(a) is different, as discussed later.

2.2. Electrical Response

Responses can be simulated using the equivalent circuit model, with the resonant frequency ω_0 chosen to match the Larmor frequency ω_L for protons in a 3T field (127.7 MHz). To correspond with test arrangements, the source is assumed to be at the proximal end, with an additional inductive probe near the tip to detect the signal as shown in Figure 2(c). Assuming a probe with resistance R_P and inductance L_P connected to a load Z_0, and a mutual inductance M_P to the last element, the equations

for the currents $I_0 \ldots I_{N+1}$ and I_P at angular frequency ω are:

$$(Z_0 + R/2 + j\omega L/2 + 1/2j\omega C)I_0 + j\omega M''I_1 = V_S$$
$$(R + j\omega L + 1/j\omega C)I_1 + j\omega M''I_0 + j\omega M I_2 = 0$$
$$(R + j\omega L + 1/j\omega C)I_n + j\omega M(I_{n-1} + I_{n+1}) = 0 \ (n = 2 \ldots N-1)$$
$$(R + j\omega L + 1/j\omega C)I_N + j\omega M I_{N-1} + j\omega M'I_{N+1} = 0 \tag{1}$$
$$(R + j\omega L + 1/j\omega C)I_{N+1} + j\omega M'I_N + j\omega M_P I_P = 0$$
$$(Z_0 + R_P + j\omega L_P)I_P + j\omega M_P I_{N+1} = 0$$

Eq. (1) is obtained by applying Kirchhoff's voltage law around each loop. The first equation describes coupling between a resonant coupling transducer containing a voltage source of impedance Z_0 and the first element of the cable section. The second describes coupling of the first element of the cable to the transducer and to the second element. The third is a recurrence relation that describes coupling of each element in the uniform cable section to its nearest neighbours. The fourth describes coupling between the last element in the cable to the second last and to the resonant tip. The fifth describes coupling between the resonant tip, the cable and the probe used to model testing. The final equation describes coupling between the probe and the tip.

Solutions can be obtained by writing the equations as $\underline{V} = \underline{Z}\underline{I}$ (where $\underline{Z}$ is a matrix of impedances and $\underline{V}$ and $\underline{I}$ are column vectors of voltages and currents) and then finding the currents as $\underline{I} = \underline{Z}^{-1}\underline{V}$. The scattering parameters S_{11} and S_{21} can then be extracted by standard methods. For correspondence with experiments the MI waveguide is assumed to have $N = 19$ elements with parameters $L = 270\,\text{nH}$, $R = 2.5\,\Omega$, $C = 5.8\,\text{pF}$, and $M = 83.5\,\text{nH}$. These parameters correspond to a Q-factor $\omega_0 L/R = 85$, a coupling coefficient $\kappa = 2M/L = 0.62$ and a characteristic impedance $Z_{0M} = 67\,\Omega$. The values $R_P = 1\,\Omega$, $L_P = 27\,\text{nH}$, and $M_P = 0.2\sqrt{(LL_P)}$ were assumed for the inductive probe. Figure 3(a) shows the frequency variation of S-parameters. The response is that of a resonant detector, peaking at ω_0 and with half the Q-factor of an isolated element.

The axial current variation obtained with a source at the coil terminals can be estimated by ignoring the inductive probe, and making simplifying assumptions. Assuming that Z_{0M} is close to Z_0 and that

(a) MI Receiver, simulation

(b) MI Receiver, experiment
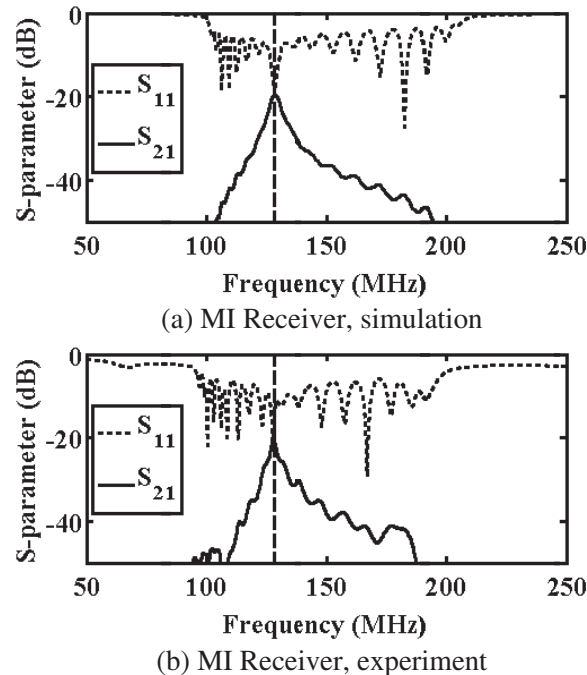
Figure 3. Frequency responses in arrangement of Figure 2(c), (a) theoretical, and (b) experimental.

loss is low, the solutions to the first five of (1) approximate at resonance to:

$$I_n = -j^n(V_S/2Z_0); \quad I_{N+1} = -j\sqrt{(Z_0/R)}I_N \tag{2}$$

Currents in adjacent elements then have equal moduli, but are 90° apart in phase, with the tip coil carrying a larger current $|I_{N+1}/I_N| = \sqrt{(Z_0/R)} \approx \sqrt{20}$, if $Z_0 = 50\,\Omega$ and $R = 2.5\,\Omega$.

3. MRI SIGNAL RECEPTION

We now consider the reception pattern, which can be estimated from reciprocity by considering the magnetic field generated with unit current at the coil terminals [34]. Generally a three-dimensional (3D) simulation is required; however, we first consider simpler 2D approximations.

3.1. 2D Model

As mentioned, the sensitivity differs at locations A ... D in Figure 2(a). Initial estimates of sensitivity can be obtained using 2D simulations. For example, at the end of the MI waveguide (B), the coil approximates to a pair of parallel wires with separation s, as in Figure 4(a). Similarly, in each section of the waveguide (A), there are two overlapping parallel wire coils, as in Figure 4(b). Approximate sensitivity variations may then be obtained as follows.
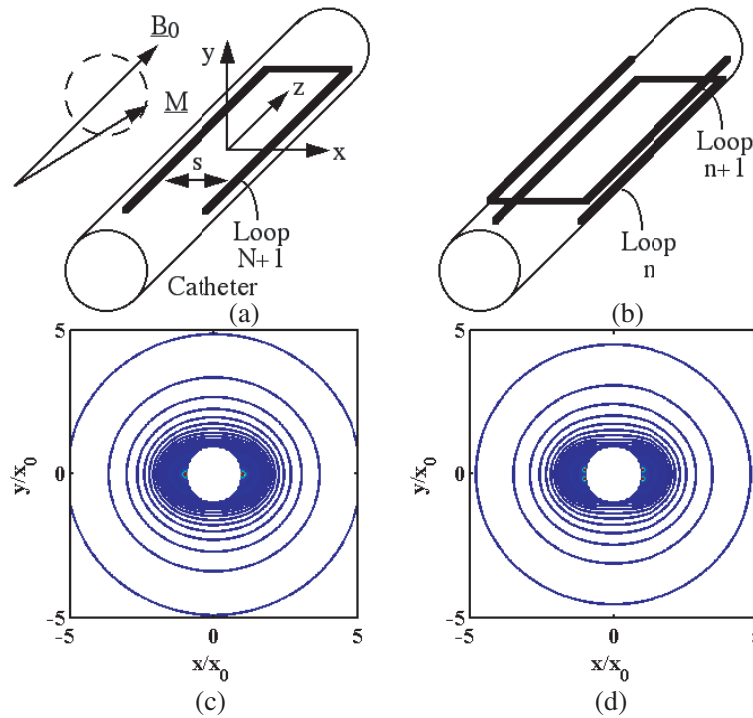
Figure 4. (a), (b) Configuration and (c), (d) 2D reception patterns for single and coupled elements.

For simplicity we assume the receiver is parallel to the z-axis, the direction of the static field B_0. The external field can then be written as $\underline{B}_{xy} = \mu_0(H_x\underline{u}_x + H_y\underline{u}_y)$, where μ_0 is the permeability of free space and $\underline{u}_x$ and $\underline{u}_y$ are unit vectors in the x- and y-directions. The complex signal voltage V_S induced in the coil by a volume dv of dipoles is then $V_S = -j\omega_L\underline{B}_{xy}.\,\underline{M}_{xy}dv$. Here $\underline{M}_{xy} = M(\underline{u}_x + j\underline{u}_y)$ is the transverse magnetization and $M = M_0$ for a 90° flip angle, where M_0 is the equilibrium magnetization per unit volume. When $\underline{H}$ is real, is simple to show that:

$$|V_S| = \omega_L\mu_0 M_0\sqrt{(H_x^2 + H_y^2)}dv \tag{3}$$

Consequently, the spatial variation of the function $\sqrt{(H_x^2 + H_y^2)}$ defines the reception pattern. For location D, we follow [9] in assuming the coil can be modeled as two cylindrical wires passing through the points $(\pm x_0, 0)$, where $x_0 = s/2$. In this case, H_x and H_y are given by:

$$H_x = -(1/2\pi)[y/\left\{(x + x_0)^2 + y^2\right\} - y/\left\{(x - x_0)^2 + y^2\right\}]$$
$$H_y = (1/2\pi)[(x + x_0)/\left\{(x + x_0)^2 + y^2\right\} - (x - x_0)/\left\{(x - x_0)^2 + y^2\right\}]$$

(4)

Figure 4(c) shows a contour map of $\sqrt{(H_x^2 + H_y^2)}$ thus obtained. At large radii, sensitivity tends to $s/2\pi r^2$, where $r^2 = x^2 + y^2$, and falls off with radial distance as $1/r^2$ [9]. This variation can be corrected by multiplying the signal intensity of axial images by a correctly-centred function $C(r^2)$ where $r^2 = (x - x_C)^2 + (y - y_C)^2$ and (x_C, y_C) is the location of the coil axis (see e.g., [3]). However, there are peaks in sensitivity near the conductors that cannot easily be corrected.

For location A, we assume that each coil can be represented as a pair of wires rotated in opposite directions by small angles about the z-axis. Each coil then generates a similarly rotated field, and the total can be found by summation. However, since the currents in adjacent coils are 90° out of phase, the combined field is complex. In this case, sensitivity depends on $\sqrt{\left\{(H_{xr} - H_{yi})^2 + (H_{yr} + H_{xi})^2\right\}}$. Figure 4(d) shows this function, which is similar to Figure 4(c) and reduces to the same function (but with a $\sqrt{2}$ increase) when the coils exactly overlap.

These results may be used to infer the sensitivity at C and D in Figure 2(a). Here the arrangement again approximates to one or two parallel wire coils. However, since the distal loop carries a larger current, it will dominate at C. Assuming the circuit parameters of the previous section, the relative sensitivity at A, B, C and D will follow the pattern $\sqrt{2}$, 1, $\sqrt{20}$, $\sqrt{20}$. Thus, sensitivity will vary longitudinally, with a small reduction at B and an increase at C and D, the distal loop. The effect of loss is to decrease sensitivity gradually along the receiver [26].

3.2. 3D Model

The reception pattern was verified using the full-wave frequency-domain finite element package COMSOL Multiphysics®(COMSOL Inc., Burlington, MA). All components were modelled as flat elements, using two layers of metal, a single layer of dielectric with $\varepsilon_r = 3.5$ extending just beyond the circuit and a dielectric surround with $\varepsilon_r = 1$. Copper tracks were modelled as impedance boundary conditions with conductivity $\sigma = 5.96 \times 10^7$ S/m. Design was based on the CAD layout used for PCB fabrication, with the loop width reduced to match the endoscope diameter. The dielectric thickness was adjusted to give the correct coupling coefficient and the capacitor length was then tuned to give the correct resonant frequency. To lower computational load, the number of resonant elements was reduced to 8. Figure 5(a) shows the simulated layout. The structure was surrounded by a cylinder of radius 100 mm and length 700 mm, with perfectly matched layer (PML) boundary conditions and tetrahedral meshing. The model was carefully checked for convergence (by varying the size of the computational domain, the meshing, and the method of modelling the metal layers) and for accuracy (by comparison with analytic results similar to those in Figures 3(a) and 4). Physical realism was verified by comparison with standard phenomena, particularly for impedance matching.

Tuning and matching followed the experimental procedure (described later). The length of the capacitors was first adjusted for operation at 127.7 MHz, using a single resonant element and a pair of inductive probes to inject and detect a suitable signal. The probes were connected to numerical lumped ports with 50 Ω impedance and S-parameters were extracted from a parametric sweep. The coupling coefficient was estimated from the resonance splitting of a pair of coupled elements. Operation of the complete circuit was then simulated, adjusting the position of the final element to halve the Q-factor of the distal resonator. Figure 5(b) shows the simulated frequency response, which shows the expected resonant response.

Finally, magnetic field components were calculated and sensitivity evaluated as a contour map of the function $\sqrt{\left\{(H_{xr} - H_{yi})^2 + (H_{yr} + H_{xi})^2\right\}}$. Figure 5(c) shows the result obtained for two different overlap values, on the sagittal $(x\text{-}y)$ plane. The first plot, with a tip element overlap of 11.4%, corresponds to the matched case. The longitudinal variation is multi-lobed, with each lobe corresponding to one half of a figure-of-eight loop. Ignoring the granularity, the sensitivity is approximately constant along the length of the cable section, reduces slightly just before the resonant tip, and rises again at the
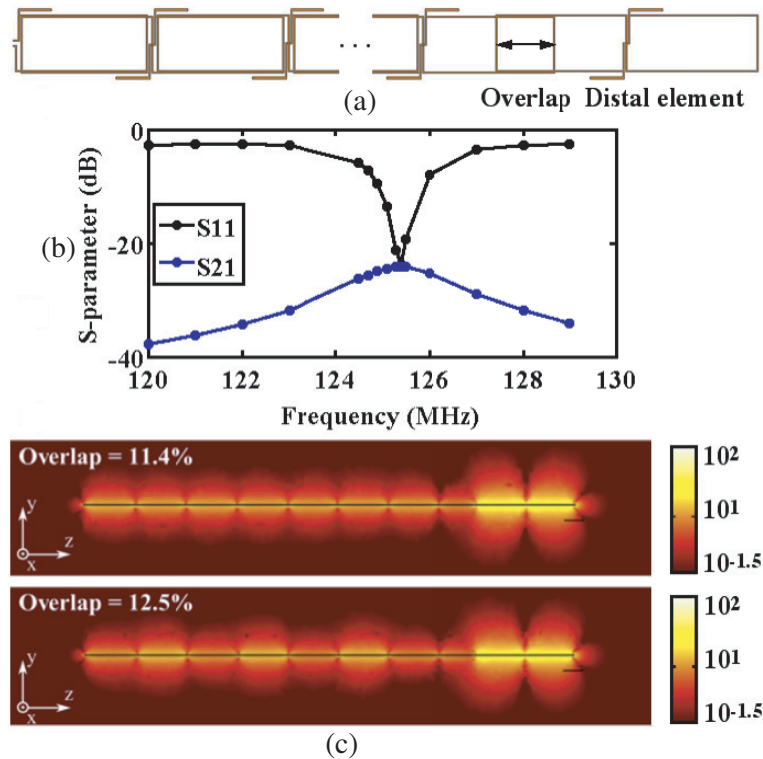
Figure 5. (a) Geometry for 3D simulation (for clarity, only metal patterns are shown); (b) Simulated variation of S-parameters for matched arrangement, and (c) sensitivity profile in the sagittal (y-z) plane, for optimally and poorly matched (11.4% and 12.5% overlap) cases.

tip as expected. The second plot illustrates the sensitivity profile for a poorly matched tip element with 12.5% overlap. In this case, a standing wave pattern can be seen along the length of the cable section.

4. CONSTRUCTION AND ELECTRICAL TESTING

We now describe assembly and bench testing. Thin-film circuits were combined with non-magnetic endoscope components. Since the main aim was to evaluate MRI compatibility and performance, most endoscopic functionality (steering, optics) was omitted to reduce cost, and circuits were mounted on the outside of the sheath to aid adjustment.

4.1. Thin Film Circuits

Thin-film circuits were fabricated by the UK company Clarydon by double-sided patterning and etching of 1 m long copper-clad Kapton® HN sheets (37.5 µm Cu + 25 µm polyimide; Dupont) [30]. Track widths of 0.5 mm and 0.75 mm were used for inductors and capacitors, respectively. Element widths (41 mm) were designed for mounting on a 13 mm diameter endoscope, while element lengths (100 mm) were made less than that of a half-wavelength ($\approx$ 130 mm at 127.7 MHz) in a dielectric constant $\varepsilon_r \approx 77$, the approximate value for tissue [14]. Circuits were formed as 19-element cables with separate transducers and final elements. Single and paired test elements were also provided to allow extraction of equivalent circuit parameters.

Electrical testing was carried out using an Electronic Network Analyzer (ENA). Individual resonators were first mounted on a 13 mm diameter cylindrical rod formed in poly ether ether ketone (PEEK). The parameter values R and L used in Section 2 were extracted by measuring the resonant frequency and Q-factor using inductive probes, with a) printed capacitors and b) capacitors of known value. The capacitor length needed to set the resonant frequency was then determined. The value of M

and the coupling coefficient κ were determined by measuring the resonance splitting of a coupled pair of elements. The position of the coupling transducer was then adjusted to minimise reflections, and set M'' correctly for matching to $50\,\Omega$. The position of the final resonator was adjusted to halve the Q-factor, and hence set M' correctly. Figure 3(b) shows the resulting frequency response, which is in good agreement with Figure 3(a).

4.2. Endoscope Components

Non-magnetic insertion tubes with the construction of Figure 1 and a diameter of $13\,\text{mm}$ were fabricated by the UK company Endoscan. The design was based on an earlier duodenoscope [6]; however, metal steering cable guides were replaced with PTFE tubing to improve RF compatibility. Capacitors were trimmed, excess Kapton was removed to enhance flexibility and circuits were mounted on insertion tubes as shown in Figure 6. Single resonators performed less well, with a reduction in Q-factor from 85 to 50 due to dielectric loss in the sheath. Despite this, the frequency response was similar to that in Figure 3(b).
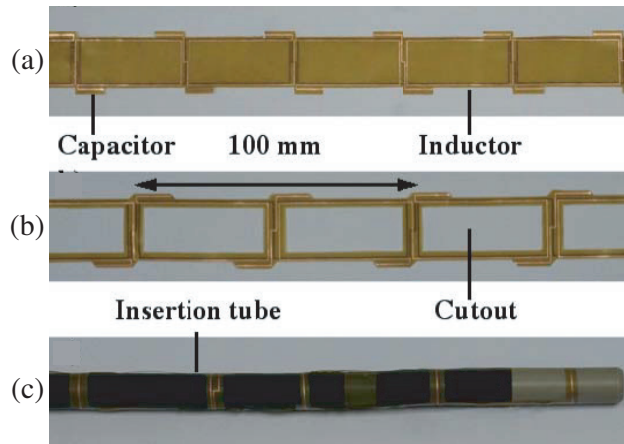
Figure 6. Thin-film circuit after (a) frequency tuning, (b) Kapton cutout and (c) mounting.

5. MAGNETIC RESONANCE IMAGING

We now describe imaging experiments carried out on a 3T GE MR750 scanner. Three types of phantom were used, the first two for imaging and the third for RF heating experiments. The first were liquid-filled tanks, designed for high-field operation and based on silicone oil doped with gadolinium beta-diketonate; these gave excellent image uniformity, but reduced loading. The second were phantoms designed for lower fields and based on water doped with $NiCl_2$ and NaCl and; these mimicked tissue loading better but gave reduced image uniformity due to standing waves. The third was a solid immersion phantom based on agar gel, designed to avoid the temperature-equalizing effects of convection currents during RF heating.
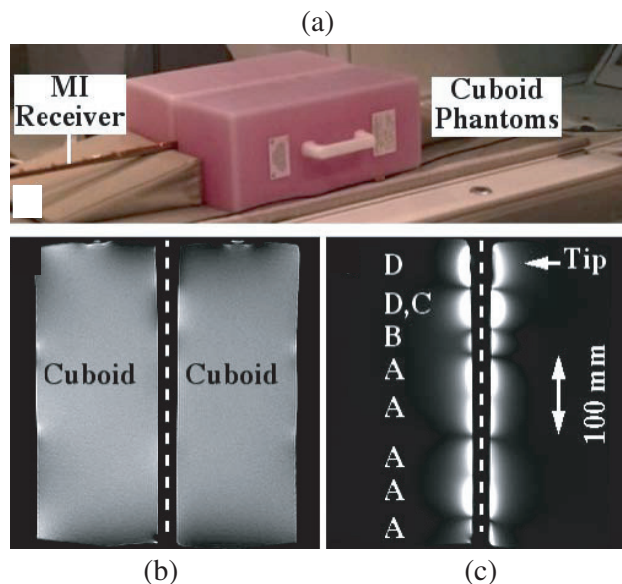
5.1. Arrangement for Imaging

Receivers were evaluated on PEEK scaffolds and on non-magnetic insertion tubes. In each case, the receiver was placed between two cuboid phantoms, in a straight or sigmoidal path (for the flexible tube) approximately parallel to the magnet bore. No magnetic effects were observed from the mechanical components. The body coil was used for excitation, and an 8-channel cardiac array coil for comparison of SNR. When used for reception, the MI receiver was connected to the auxiliary coil input, with a PIN diode across its terminals to enable the coil identification test; otherwise, it was connected to a $50\,\Omega$ load. Imaging was carried out using spin echo sequences, with a $90°$ flip angle, an excitation time

TE = 10 ms, a repetition time TR = 500 ms, 100% phase field of view (FOV), a 256 × 256 acquisition matrix and a single excitation.

5.2. Field-of-View

Figure 7(a) shows the arrangement for evaluating a receiver on a PEEK rod using high-field phantoms. Figure 7(b) shows a coronal slice image passing through the centre of the receiver, obtained using the body coil with a slice thickness of 5 mm, a slice separation of 13 mm and a FOV of 380 mm. Both phantoms can be seen, with approximately uniform brightness. There is little perturbation to the magnetization near the receiver (the dashed track), suggesting that effective decoupling is provided by its figure-of-eight element layout. Figure 7(c) shows the image obtained using the MI receiver itself. Useful signal is now only generated near the axis, and the FOV displays the segmentation shown in Figure 5(c). The predicted sensitivity variation can be seen, with uniform brightness at A, a decrease at B and an increase at C and D, the distal tip.
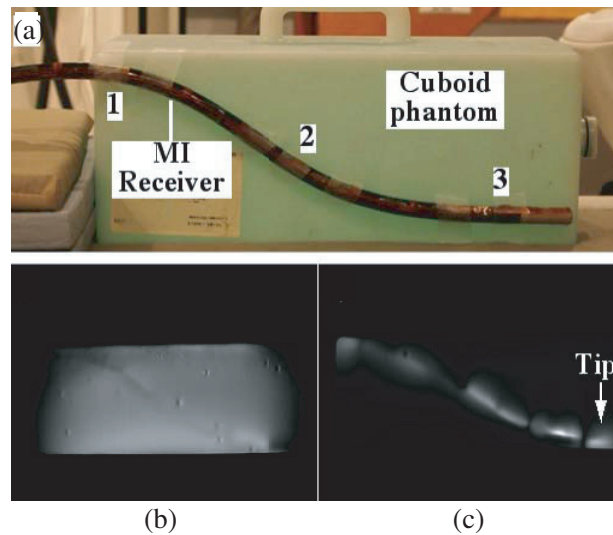

Figure 7. (a) Arrangement for imaging of high-field phantoms using a rod mounted magneto-inductive receiver; (b) and (c) Coronal images obtained using the body coil and MI receiver.

Figure 8(a) shows the arrangement for evaluating a MI receiver on an insertion tube using low-field phantoms, with the array coil for comparison. Figure 8(b) shows an axial slice through the distal loop, obtained using the array coil with a slice thickness of 5 mm, a slice separation of 8.5 mm and a FOV of 160 mm. Half of each cuboid may be seen. The image brightness is again roughly uniform, and there is no evidence of susceptibility mismatch, but standing wave effects are now evident. However, there is little perturbation to the magnetization due to the receiver (the circle). Figure 8(c) shows the corresponding image obtained using the MI receiver. The restricted FOV is again apparent, as is the local increase in brightness.

Figure 9(a) shows a similar arrangement, with the endoscope now bent into a sigmoidal path. Once again, the array coil has been used for comparison. Figure 9(b) shows a sagittal slice through the edge of one cuboid, obtained using the array coil with a slice thickness of 5 mm, a slice separation of 5.5 mm and a FOV of 400 mm. The image brightness is clearly reduced at either end of the cuboid, due to the restricted length of the array, and some minor perturbation to the magnetization may be seen following the track of the endoscope. Figure 9(c) shows the image obtained using the MI receiver. The FOV now follows that path of the tube, confirming the receiver's ability to operate well even when bent.
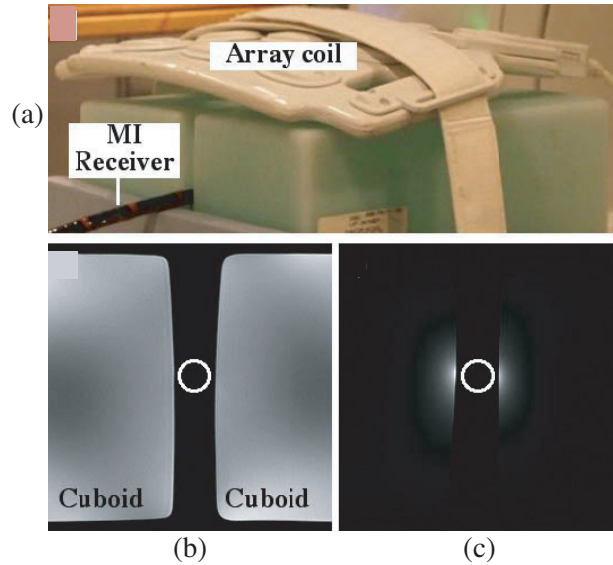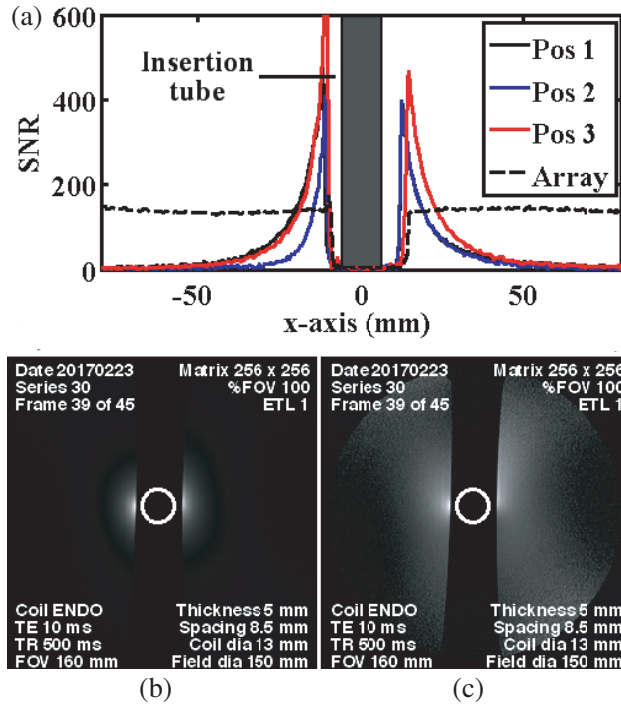
Figure 8. (a) Arrangement for imaging of low-field phantoms using a tube mounted magneto-inductive receiver; (b) and (c) Axial images obtained using the array coil and MI receiver.

Figure 9. (a) Arrangement for imaging of low-field phantoms using a flexed, tube-mounted magneto-inductive receiver; (b) and (c) Sagittal images obtained using the array coil and MI receiver.

5.3. Signal-to-Noise Ratio

Figure 7 suggests that the MI receiver has a SNR advantage, up to around 6 times the endoscope radius. However, this example is unrealistic, since the receiver is straight, the loading is light and the benchmark (the body coil) has low performance. A more realistic comparison is obtained between a flexed, tube-mounted MI receiver and the array coil using low-field phantoms, for example as in Figure 9(a). Figure 10(a) compares the numerical variation of SNR in the horizontal direction, obtained from axial slices as the ratio of signal to the standard deviation of noise in a region without signal. For the array coil, a single representative variation (dashed) is shown, which yields a uniform SNR of ≈ 120. For the MI receiver, variations are shown for slices at 1, 2 and 3 (full lines). In each case, SNR falls off approximately as $1/x^2$. Peak SNR is high, especially in slice 3, and here performance exceeds the array to around three times the endoscope radius.

Figure 10. (a) Comparison of the spatial variation of SNR in axial slice images obtained using the array coil and the curved, tube-mounted magneto-inductive receiver; (b) and (c) Axial slice images obtained using the MI receiver, before and after correction for the radial sensitivity variation.

5.4. Image Correction

Finally, Figures 10(b) and 10(c) compare axial images obtained using the MI receiver, before and after correction for the radial variation in sensitivity. To avoid amplifying noise in regions far away from the coil, the following correction was used:

$$C(r^2) = (r/r_c)^2 / \left\{1 - a + a(r/r_c)^2\right\} \tag{5}$$

Here r_c is the coil radius and a is an adjustable constant, typically $\ll 1$. This function tends to zero at $r = 0$ and unity at $r = r_c$, and saturates at $1/a$ for large r. Figure 10(b) shows the uncorrected image and Figure 10(c) the result obtained with $a = 0.05$. The corrected image clearly has a more uniform brightness, but little can be done to reduce the sensitivity peaks near the conductors.

5.5. MRI Safety

Experiments aimed at clarifying the potential for RF-induced heating were also carried out, by lengthy imaging in an immersion phantom. To prepare the phantom, agar (45 g/L) was dissolved in hot water and mixed with n-propanol (82.8 ml/L), glycerol (300 ml/L) and a salt solution (617 ml/L). The latter contained $NiCl_2 \cdot 6H_2O$ (3.37 g/L) and NaCl (2.4 g/L), giving liver mimicking MR properties ($T_1 = 800$ ms, $T_2 = 50$ ms). Dielectric properties were verified as $\sigma = 0.33$ S/m, $\varepsilon_r = 77.49$, by measurement at 127.7 MHz with a dielectric probe (85070E, Keysight Technologies).

A further MI receiver was mounted on a PEEK rod using 13 mm diameter heat shrink tube and held horizontally in the middle of a 1.5 metre-long Perspex tank divided into five compartments. Four were filled with gel; however, to allow connection and testing, the proximal compartment containing the transducer was left unfilled. A total of 12.5 L of gel was required, prepared and cast in three batches. Four fibre optic thermometers (Luxtron 790, Luxtron, Santa Clara, CA) were used for temperature monitoring. Three were mounted at the proximal (L1), midpoint (L2) and distal (L3) points of the immersed section of receiver, with the fourth (L4) just beyond the distal tip. Figure 11(a) shows the arrangement on the patient bed.

Metrology was first carried out using the body coil for excitation and the MI receiver for reception. The inset to Figure 11(a) shows an axial image obtained with a spin echo sequence, without correction for radial sensitivity, showing that a sensor (arrowed) has been correctly located. Heating was then carried out using repetitive application of a RF-intensive Turbo spin echo sequence while monitoring the temperature. Figure 11(b) shows the time evolution of temperature at the locations L1–L4. The left hand traces show results obtained while heating for 15 mins with a specific absorption rate (SAR) of 0.4 W/kg. Apart from a known calibration error in L4, there is little to note other than a slow decrease in temperature as the gel cooled in the magnet room. The SAR was then increased to 0.5 W/kg and heating was repeated for a further 20 mins. Once again, no temperature rise was observed. Although these experiments involve a single immersed length, the results suggest an encouraging lack of sensitivity to RF heating.
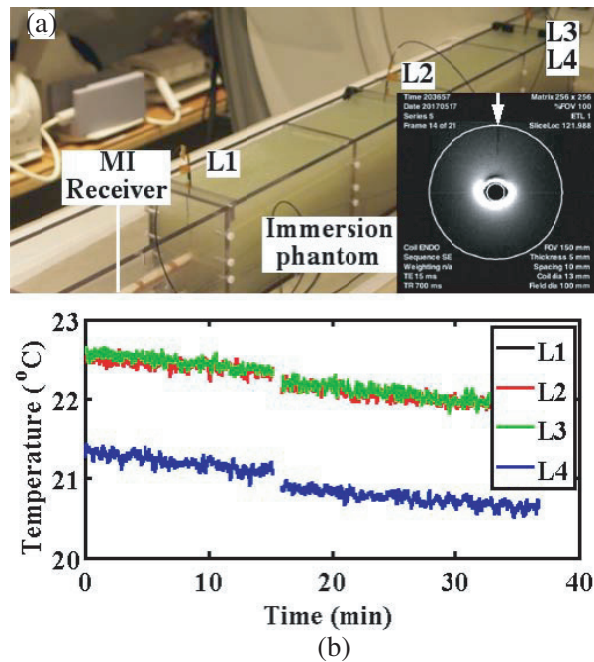
Figure 11. (a) Arrangement for RF heating in a gel phantom, showing the location of the MI endoscope and the four sensors. Inset: Uncorrected axial image, with an arrow indicating a sensor track; (b) Time evolution of temperatures at L1-L4, during two periods of RF heating.

6. CONCLUSIONS

An early prototype MRI duodenoscope capable of ^{1}H imaging at 3T along its length has been demonstrated, by combining non-magnetic endoscope components with a thin film magneto-inductive receiver. The receiver is designed for mounting in the sheath, leaving other functionality unaltered. The circuit consists of a magnetically coupled array of L-C resonators formed by patterning copper-clad Kapton with figure-of-eight inductors and parallel plate capacitors. The twisted inductor shape provides decoupling against B_1 fields, while the segmentation avoids electrically induced heating. Predictions of electrical performance and detection sensitivity have been verified by experiment. The FOV is a segmented coaxial cylinder, with a sensitivity that falls off radially as $1/r^2$. Phantom experiments show a peak SNR gain compared with an 8-element array to three times the diameter of the endoscope. Initial gel-based immersion imaging tests have been carried out to confirm RF safety. However, further work is required to investigate flexibility and reliability, RF compatibility with metal components such as guide-wires, and further safety tests following construction of a complete instrument.

ACKNOWLEDGMENT

REFERENCES

1. Hoult, D. I. and P. C. Lauterbur, "The sensitivity of the zeugmatographic experiment involving human samples," *J. Magn. Reson.*, Vol. 34, 425–433, 1979.

2. Ocali, O. and E. Atalar, "Ultimate intrinsic signal-to-noise ratio in MRI," *Magn. Reson. Med.*, Vol. 39, 462–473, 1988.

3. Eryaman, Y., Y. Oner, and E. Atalar, "Design of internal coils using ultimate intrinsic SNR," *Magn. Reson. Mater. Phys.*, Vol. 22, 221–228, 2009.

4. Inui, K., S. Nakazawa, J. Yoshino, et al., "Endoscopic MRI: Preliminary results of a new technique for visualization and staging of gastrointestinal tumors," *Endoscopy*, Vol. 27, 480–485, 1995.

5. Gilderdale, D. J., A. D. Williams, U. Dave, and N. M. de Souza, "An inductively-coupled, detachable receiver coil system for use with magnetic resonance compatible endoscopes," *JMRI*, Vol. 18, 131–135, 2003.

6. Syms, R. R. A., I. R. Young, C. A. Wadsworth, S. D. Taylor-Robinson, and M. Rea, "Magnetic resonance imaging duodenoscope," *IEEE Trans. Biomed. Engng.*, Vol. 60, 3458–3467, 2013.

7. Kantor, H. L., R. W. Briggs, and R. S. Balaban, "In vivo ^{31}P nuclear magnetic resonance measurements in canine heart using a catheter-coil," *Circ. Res.*, Vol. 55, 261–266, 1984.

8. Martin, P. J., D. B. Plewes, and R. M. Henkelman, "MR imaging of blood vessels with an intravascular coil," *J. Magn. Reson. Imag.*, Vol. 2, 421–429, 1992.

9. Atalar, E., P. A. Bottomley, O. Ocali, L. C. L. Correia, M. D. Kelemen, J. A. C. Lima, and E. A. Zerhouni, "High resolution intravascular MRI and MRS by using a catheter receiver coil," *Magn. Reson. Med.*, Vol. 36, 596–605, 1996.

10. Bottomley, P. A., E. Atalar, R. F. Lee, K. A. Shunk, and A. Lardo, "Cardiovascular MRI probes for the outside in and for the inside out," *Magn. Reson. Mats. Phys. Biol. Med.*, Vol. 11, 49–51, 2000.

11. Duerk, J. L., E. Y. Wong, and J. S. Lewin, "A brief review of hardware for catheter tracking in magnetic resonance imaging," *MAGMA*, Vol. 13, 199–208, 2002.

12. Boskamp, E., "Improved surface coil imaging in MRI: Decoupling of the excitation and receiver coils," *Radiology*, Vol. 157, 449–452, 1985.

13. Nitz, W. R., A. Oppelt, W. Renz, C. Manke, M. Lenhart, and J. Link, "On the heating of linear conductive structures as guidewires and catheters in interventional MRI," *J. Magn. Reson. Imag.*, Vol. 13, 105–114, 2001.

14. Atalar, E., "Safe coaxial cables," *Proc. 7th Ann. Meet. ISMRM*, 1006, Philadelphia, PA, USA, May 24–28, 1999.

15. Ladd, M. E. and H. H. Quick, "Reduction of resonant RF heating in intravascular catheters using coaxial chokes," *Magn. Reson. Med.*, Vol. 43, 615–619, 2000.

16. Vernickel, P., V. Schulz, S. Weiss, and B. Gleich, "A safe transmission line for MRI," *IEEE Trans. Biomed. Engng.*, Vol. 52, 1094–1102, 2005.

17. Krafft, A., S. Müller, R. Umathum, W. Semmler, and M. Bock, "B_1 field-insensitive transformers for RF-safe transmission lines," *Magn. Reson. Mater. Phys.*, Vol. 19, 257–266, 2006.

18. Wiltshire, M. C. K., J. V. Hajnal, J. B. Pendry, D. J. Edwards, and C. J. Stevens, "Metamaterial endoscope for magnetic field transfer: Near field imaging with magnetic wires," *Optics Express*, Vol. 11, 709–714, 2003.

19. Freire, M. J. and R. Marques, "Planar magnetoinductive lens for three-dimensional subwavelength imaging," *Appl. Phys. Letts.*, Vol. 86, art. 182505, 2005.

20. Freire, M. J., R. Marques, and L. Jelinek, "Experimental demonstration of a $\mu_r = -1$ metamaterial lens for magnetic resonance imaging," *Appl. Phys. Lett.*, Vol. 93, 231108, 2008.

21. Schelekova, A. V., A. P. Slobozhanyuk, S. B. Glybovski, et al., "Application of metasurfaces for magnetic resonance imaging," *Proc. 10th Metamaterials Conf.*, 13–14, Platanias, Crete, Sept. 17–22, 2016.

22. Slobozhanyuk, A. P., A. N. Poddubny, A. J. E. Raaijmakers, et al., "Enhancement of magnetic resonance imaging with metasurfaces," *Adv. Mats.*, Vol. 28, 1832–1838, 2016.

23. Belov, P. A. and Y. Hao, "Subwavelength imaging at optical frequencies using a transmission device formed by a periodic metal-dielectric structure operating in the canalization regime," *Phys. Rev. B*, Vol. 73, 113110, 2006.

24. Radu, X., D. Garray, and C. Craeye, "Towards a wire medium endoscope for MRI imaging," *Metamaterials*, Vol. 3, 90–99, 2009.

25. Belov, P. A., G. K. Palikaras, Y. Zhao, et al., "Experimental demonstration of multiwire endoscopes capable of manipulating near-fields with sub-wavelength resolution," *Appl. Phys. Lett.*, Vol. 97, 191905, 2010.

26. Syms, R. R. A., I. R. Young, M. M. Ahmad, and M. Rea, "Magnetic resonance imaging with linear magneto-inductive waveguides," *J. Appl. Phys.*, Vol. 112, 114911, 2012.

27. Syms, R. R. A., I. R. Young, M. M. Ahmad, S. D. Taylor-Robinson, and M. Rea, "Magneto-inductive catheter receiver for magnetic resonance imaging," *IEEE Trans. Biomed. Engng.*, Vol. 60, 2421–2431, 2013.

28. Segkhoonthod, K., R. R. A. Syms, and I. R. Young, "Design of magneto-inductive magnetic resonance imaging catheters," *IEEE Sensors J.*, Vol. 14, 1505–1513, 2014.

29. Kardoulaki, E., R. R. A. Syms, I. R. Young, and M. Rea, "SNR in MI catheter receivers for MRI," *IEEE Sensors J.*, Vol. 16, 1700–1707, 2016.

30. Syms, R. R. A., I. R. Young, L. Solymar, and T. Floume, "Thin-film magneto-inductive cables," *J. Phys. D. Appl. Phys.*, Vol. 43, 055102, 2010.

31. Syms, R. R. A., L. Solymar, and I. R. Young, "Broad-band coupling transducers for magneto-inductive cable," *J. Phys. D. Appl. Phys.*, Vol. 43, 285003, 2010.

32. Shamonina, E., V. A. Kalinin, K. H. Ringhofer, and L. Solymar, "Magneto-inductive waveguide," *Elect. Lett.*, Vol. 38, 371–373, 2002.

33. Wiltshire, M. C. K., E. Shamonina, I. R. Young, and L. Solymar, "Dispersion characteristics of magneto-inductive waves: Comparison between theory and experiment," *Elect. Lett.*, Vol. 39, 215–217, 2003.

34. Hoult, D. I. and R. E. Richards, "The signal-to-noise ratio of the nuclear magnetic resonance experiment," *J. Magn. Reson.*, Vol. 24, 71–85, 1976.